



HAL
open science

Human cerebral organoids reveal progenitor pathology in EML1-linked cortical malformation

Ammar Jabali, Anne Hoffrichter, Ana Uzquiano, Fabio Marsoner, Ruven Wilkens, Marco Siekmann, Bettina Bohl, Andrea C Rossetti, Sandra Horschitz, Philipp Koch, et al.

► **To cite this version:**

Ammar Jabali, Anne Hoffrichter, Ana Uzquiano, Fabio Marsoner, Ruven Wilkens, et al.. Human cerebral organoids reveal progenitor pathology in EML1-linked cortical malformation. *EMBO Reports*, 2022, 23, 10.15252/embr.202154027 . hal-03872626

HAL Id: hal-03872626





<https://hal.sorbonne-universite.fr/hal-03872626>

Submitted on 25 Nov 2022

HAL is a multi-disciplinary open access archive for the deposit and dissemination of scientific research documents, whether they are published or not. The documents may come from teaching and research institutions in France or abroad, or from public or private research centers.

L'archive ouverte pluridisciplinaire **HAL**, est destinée au dépôt et à la diffusion de documents scientifiques de niveau recherche, publiés ou non, émanant des établissements d'enseignement et de recherche français ou étrangers, des laboratoires publics ou privés.

Human cerebral organoids reveal progenitor pathology in *EML1*-linked cortical malformation

Ammar Jabali^{1,2,3,4}, Anne Hoffrichter^{1,2,3} , Ana Uzquiano^{5,6,7}, Fabio Marsoner^{1,2,3}, Ruven Wilkens^{1,2,3}, Marco Siekmann^{1,2,3}, Bettina Bohl^{1,2,3} , Andrea C Rossetti^{1,2,3}, Sandra Horschitz^{1,2,3}, Philipp Koch^{1,2,3}, Fiona Francis^{5,6,7}  & Julia Ladewig^{1,2,3,4,*} 

Abstract

Malformations of human cortical development (MCD) can cause severe disabilities. The lack of human-specific models hampers our understanding of the molecular underpinnings of the intricate processes leading to MCD. Here, we use cerebral organoids derived from patients and genome edited-induced pluripotent stem cells to address pathophysiological changes associated with a complex MCD caused by mutations in the echinoderm microtubule-associated protein-like 1 (*EML1*) gene. *EML1*-deficient organoids display ectopic neural rosettes at the basal side of the ventricular zone areas and clusters of heterotopic neurons. Single-cell RNA sequencing shows an upregulation of basal radial glial (RG) markers and human-specific extracellular matrix components in the ectopic cell population. Gene ontology and molecular analyses suggest that ectopic progenitor cells originate from perturbed apical RG cell behavior and yes-associated protein 1 (YAP1)-triggered expansion. Our data highlight a progenitor origin of *EML1* mutation-induced MCD and provide new mechanistic insight into the human disease pathology.

Keywords *EML1*; malformation of human cortical development; cerebral organoids; perturbed progenitor cells; YAP1 signaling

Subject Categories Molecular Biology of Disease; Neuroscience

DOI 10.15252/embr.202154027 | Received 20 September 2021 | Revised 11 February 2022 | Accepted 17 February 2022 | Published online 15 March 2022

EMBO Reports (2022) 23: e54027

Introduction

Human cortical expansion and lamination relies on the intrinsic organization and behavior of RG cells and precise neuronal migration (Lui *et al.*, 2011). Disruption of these processes can cause MCD including microcephaly (small brain), megalencephaly (large brain),

lissencephaly (loss of gyrification), polymicrogyria (numerous small gyrifications), and heterotopia (abnormally positioned neurons) (Klingler *et al.*, 2021). These abnormalities can coexist in complex forms. For example, individuals carrying a mutation in the *EML1* gene (coding for a microtubule-associated protein (Richards *et al.*, 2015)) exhibit megalencephaly with a polymicrogyria-like cortex above a ribbon-like subcortical heterotopia (rl-SH) in the region of the former outer subventricular zone (SVZ), resembling a second inner cortex (Kielar *et al.*, 2014; Oegema *et al.*, 2019). Patients can also exhibit hydrocephalus (Shaheen *et al.*, 2017). *EML1*-patients suffer from severe developmental delay, often drug-resistant epilepsy, visual impairment, and intellectual disabilities (Kielar *et al.*, 2014; Shaheen *et al.*, 2017; Oegema *et al.*, 2019). *Eml1* mouse models show ectopic proliferating cells in the developing cortical wall, perturbed apical RG cell behavior, and aberrant primary cilia (Kielar *et al.*, 2014; Bizzotto *et al.*, 2017; Uzquiano *et al.*, 2019). Although they exhibit heterotopia, they fall short of recapitulating the complete spectrum of phenotypes observed in humans such as a polymicrogyria-like cortex or megalencephaly (Kielar *et al.*, 2014; Collins *et al.*, 2019), highlighting differences in disease manifestation between humans and non-human model organisms. Here, we explore the function of *EML1* during cortical development using human-induced pluripotent stem (iPS) cells and thereof derived cortical cultures.

Results and Discussion

EML1-deficient cerebral organoids exhibit subcortical heterotopia-like phenotypes

To dissect the molecular role of *EML1* underlying human cortical development and associated disorders, we reprogrammed fibroblasts from two independent previously characterized patients harboring mutations in the *EML1* gene (for more details see Material and Methods and (Kielar *et al.*, 2014)) into iPS cells (two clones

1 Medical Faculty Mannheim, Central Institute of Mental Health, Heidelberg University, Mannheim, Germany

2 Hector Institute for Translational Brain Research, Mannheim, Germany

3 German Cancer Research Center, Heidelberg, Germany

4 Institute of Reconstructive Neurobiology, School of Medicine & University Hospital Bonn, University of Bonn, Bonn, Germany

5 INSERM U 1270, Paris, France

6 Sorbonne Université, UMR-S 1270, Paris, France

7 Institut du Fer à Moulin, Paris, France

*Corresponding author. Tel: +49621 1703 6091; E-mail: julia.ladewig@zi-mannheim.de

each; characterization of iPS cells is illustrated in Fig EV1A and B). *EML1* patient-specific mutations (patient 1, compound heterozygous, R138X, T243A; patient 2, homozygous, and W225R) were confirmed by sequencing (Fig EV1C and D). To decipher the specific role of *EML1* in an isogenic system, we also generated heterozygous *EML1*-knockout (*EML1*-heKO) iPS cells from two independent controls by applying CRISPR-Cas9 genome editing. Of note: homozygous *EML1*-KO clones were prone to die and could not be further cultured. *EML1*-heKO lines were validated by genotyping (Fig EV1E). Reduced expression of *EML1* was confirmed for both *EML1*-heKO lines (Fig EV1F). We then differentiated iPS cells into cortical progenitors (Shi *et al*, 2012) and forebrain organoids (Iefremova *et al*, 2017; Krefft *et al*, 2018). To investigate whether certain *EML1* mutation-induced phenotypic changes are recapitulated within cerebral organoids, we first analyzed patient- and control-derived organoids at day 33 ± 2 , the time point at which cerebral organoids have developed ventricular zone (VZ)-, SVZ-, and cortical plate (CP)-like areas as well as cells reminiscent of basal (b)RG (Iefremova *et al*, 2017). Immunocytochemical analyses revealed that control organoids consist of stratified structures including VZ and CP areas (Fig 1A). In strong contrast, *EML1* patient-derived organoids exhibited massive amounts of ectopically localized cells accumulating at the basal side of the VZ areas, in part organized into neural rosettes with accumulation of adherent junction markers such as N-cadherin (NCAD) in their centers (Fig 1B). In addition, β -III-tubulin-positive neurons were organized in two bands, an upper diffuse band located above the ectopic cells and a lower band located in between the VZ area and the ectopic cell population (Fig 1A). To assess the phenotypic changes in all *EML1*-deficient conditions (*EML1*-patient 1, *EML1*-patient 2, *EML1*-heKO 1, and *EML1*-heKO 2), we performed immunohistochemistry and quantified the percent of VZ areas with ectopically localized neural rosettes and the percent of heterotopic or disorganized cortical areas in control and *EML1*-deficient organoids. We confirm a significant increase in neural rosettes and heterotopic clusters of MAPT-positive neurons in all *EML1*-deficient organoids compared to controls (Fig 1C–E, day 20 ± 2).

Perturbed cell intrinsic properties of *EML1*-deficient apical radial glial cells

To understand the origin of the perturbed ectopic cell population in the *EML1*-deficient organoids, we examined RG cell behavior in

more detail in *EML1*-deficient and control organoids at early developmental time points (day 20 ± 2). *EML1*-deficient *in vivo* and *in vitro* models show changes in microtubule-associated processes including mitotic spindle length, cell shape, and primary cilia (Bizzotto *et al*, 2017; Uzquiano *et al*, 2019). It was suggested that the changes in spindle length and cell morphology might cause increased mechanical stress in the VZ and by that indirectly encourage RG cell delamination (Bizzotto *et al*, 2017). To test whether a non-cell autonomous mechanism leads to the accumulation of ectopic progenitor cells in *EML1*-deficient organoids, we generated hybrid organoids composed of EGFP-*EML1*-heKO or EGFP-control iPS cells mixed with isogenic control iPS cells before organoid generation. When investigating the hybrid organoids at day 20 ± 2 , we found a significant increase in the number of EGFP-positive *EML1*-heKO cells at the basal side of VZ areas compared to the controls (Fig 2A and B). These data hint toward cell intrinsic mechanisms leading to the ectopic progenitor cells in *EML1*-deficient organoids. It has been shown that changes in the mitotic spindle and primary cilia can directly impact division mode and RG cell delamination (LaMonica *et al*, 2013; Mora-Bermúdez *et al*, 2014; Bizzotto *et al*, 2017). We first tested whether the division mode is perturbed in *EML1*-impaired conditions. To that end we visualized mitotic cells (Figs 2C and EV2A) and quantified the plane of cell divisions. While in control organoids the majority of cells exhibit a vertical plane of cell division, we found a significant decrease in vertical division modes in all *EML1*-impaired conditions. In parallel, *EML1*-impaired organoids exhibit an increase in oblique and horizontal division angles (Fig 2D, day 20 ± 2). Of note, both oblique and horizontal plane of cell divisions at the VZ surface were described to favor cell delamination (LaMonica *et al*, 2013). We next investigated the primary cilium and found a significant decrease in the length of the primary cilium in all *EML1*-deficient-derived cortical progenitor cells upon ARL13B immunostaining (Figs 2E and EV2B) and confirmed perturbed ultrastructure of patient and *EML1*-heKO-derived primary cilia by electron microscopy (Fig 2F, (Uzquiano *et al*, 2019)). To investigate whether *EML1*'s microtubule function causes the observed defects in primary cilia, we stabilized microtubules in control and *EML1*-deficient cultures using EPOHiloneD (Zhang *et al*, 2012) (EpoD). Immunoblot analyses confirmed a significant increase in stabilized (acetylated) tubulin upon EpoD treatment in all *EML1*-deficient samples (Fig EV2C and D). When investigating the primary cilia in control- and *EML1*-deficient

Figure 1. Deficiency of *EML1* causes ectopic neural rosettes and neuronal heterotopia in cerebral organoids.

- A Day 33 ± 2 control- and *EML1* patient-derived cerebral organoids stained for β -III-tubulin and DAPI. VZ and CP areas are marked by white brackets, ectopic neural rosettes by red bracket, and heterotopic neurons by red arrows.
- B Day 33 ± 2 control- and *EML1* patient-derived cerebral organoid stained for the adherens junction marker N-cadherin (NCAD) expressed at the VZ surface and within the ectopic neural rosettes.
- C Day 20 ± 2 cerebral organoids derived from controls, patients, and *EML1*-heKOs stained for the neuronal marker MAPT and the adherens junction marker NCAD, counterstained with DAPI. Ectopic neural rosettes and neuronal heterotopia are highlighted with dotted yellow lines.
- D Quantification of VZ areas with ectopic neural rosettes (three batches, three organoids analyzed per batch, significance based on Kruskal–Wallis test, $P = 0.0001$, Dunn's *post hoc* test for multiple comparisons performed to define statistical differences between genotypes, and single data points presented are colored by batch).
- E Quantification of heterotopic, disorganized, or organized cortical areas (three batches, three organoids per batch, significance based on Kruskal–Wallis test, $P = 0.0001$ for "organized" and "heterotopic"; no significant difference for "disorganized," Dunn's *post hoc* test performed for multiple comparisons to define statistical differences between genotypes).

Data information: * marks statistical significance in relation to Control 1, # in relation to Control 2. *P*-values: ***/### < 0.001. VZ, ventricular zone; CP, cortical plate.

Data in graphs are represented as means \pm SD. Scale bars: (A) 100 μ m; (B) 100 μ m, enlarged 25 μ m; and (C) 50 μ m.

Source data are available online for this figure.

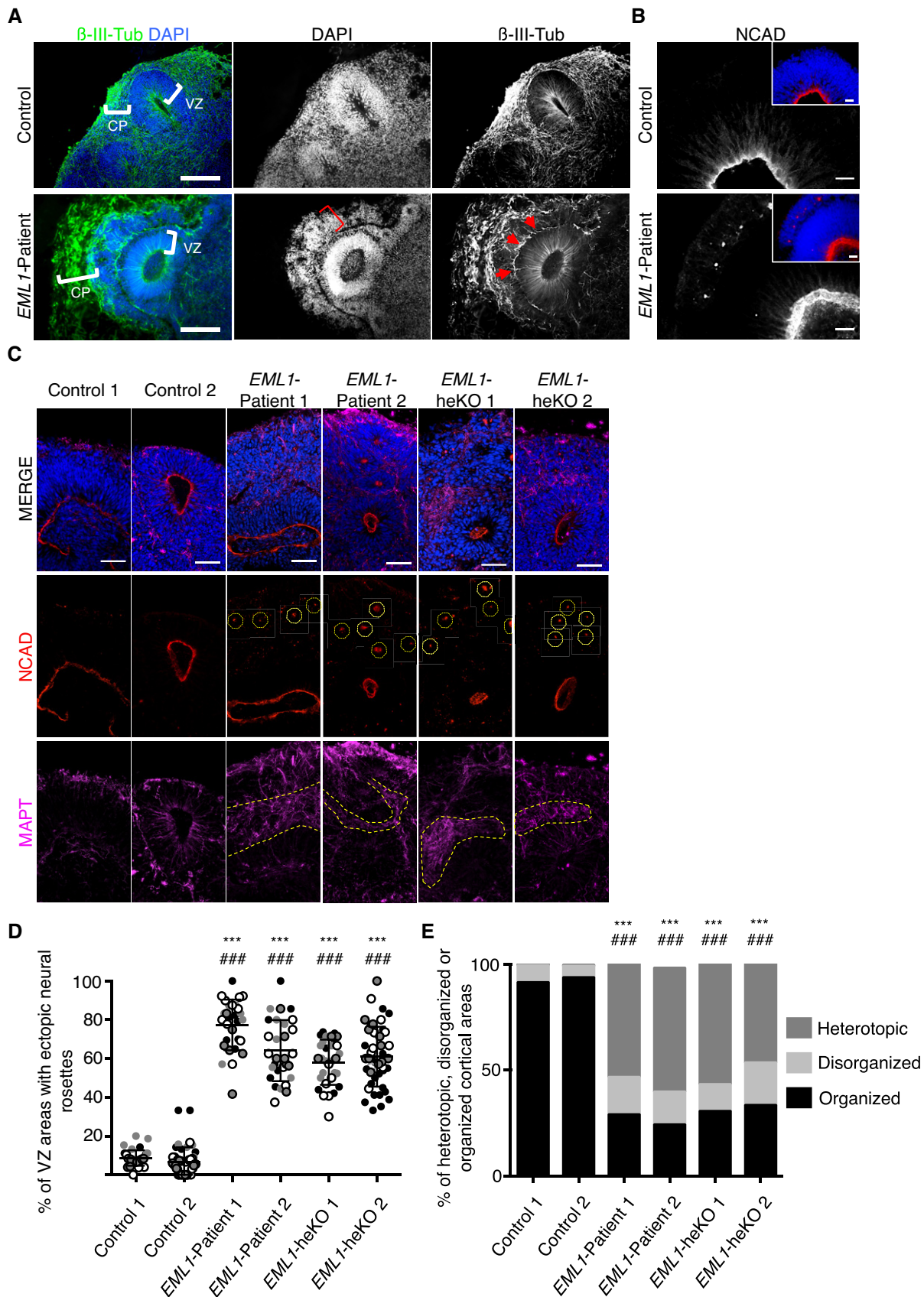


Figure 3.

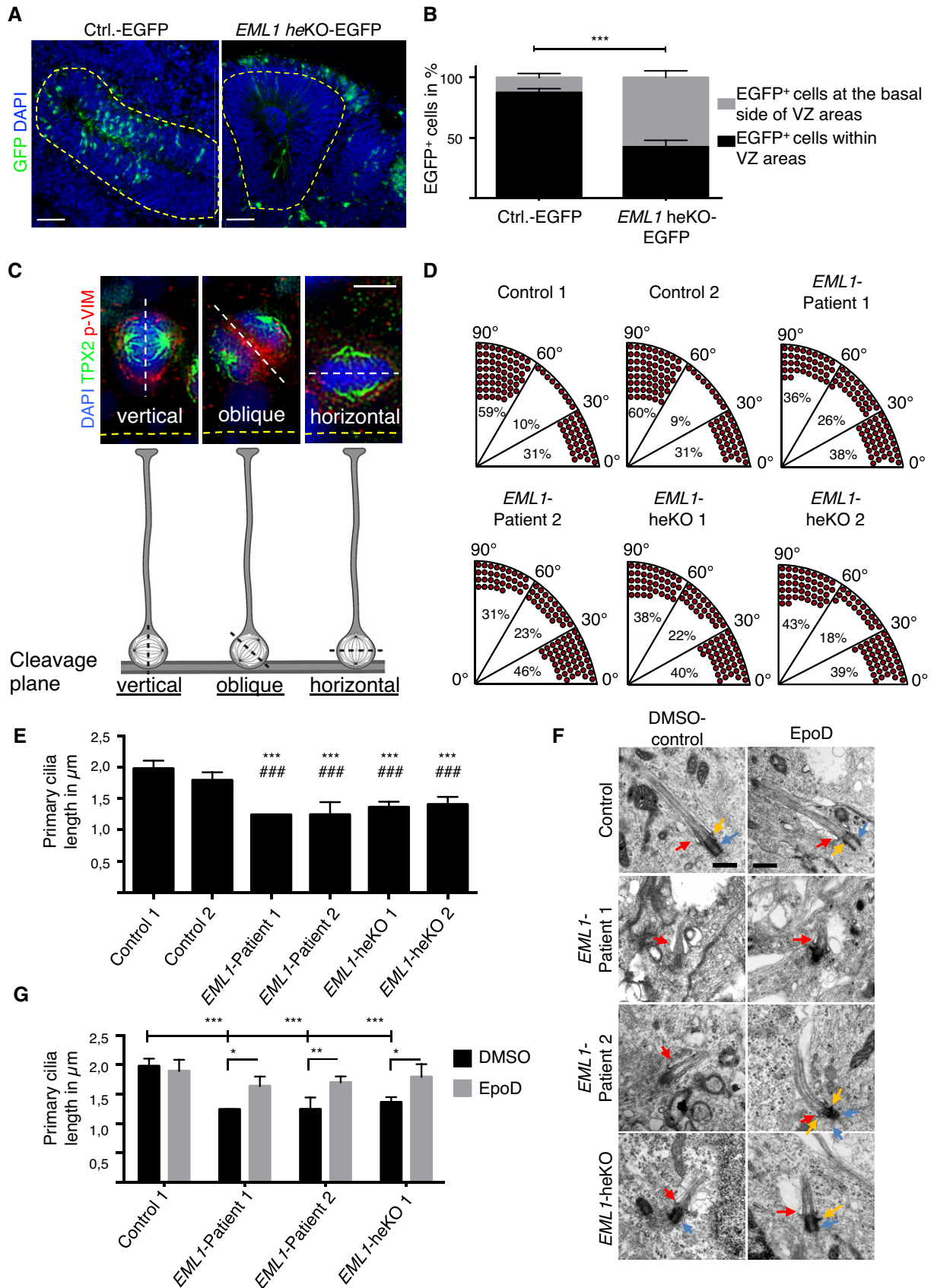


Figure 2.

Figure 2. Ectopic progenitor cells originate from apical RG with perturbed cell intrinsic behavior.

- A Hybrid organoids generated from controls mixed with control-EGFP⁺ or *EML1*-heKO-EGFP⁺ cells (day 20 ± 2). Yellow dotted lines indicate VZ areas.
- B Quantification of control-EGFP⁺ or *EML1*-heKO-EGFP⁺ cells within or at the basal side of VZ areas (three batches, three organoids each, significance based on Mann–Whitney test, ****P* = 0.0001 for “EGFP⁺ cells at the basal side of VZ areas”).
- C Representative images and scheme of cleavage plane orientation. Upper panel: cells immunostained for p-Vim (red) and TPX2 (green), counterstained with DAPI, white dotted line indicates cleavage plane orientation, and yellow dotted line VZ surface.
- D Quantification of horizontal, vertical, and oblique plane of cell divisions in control and *EML1*-deficient organoids (day 20 ± 2; three batches and three organoids each).
- E Quantification of primary cilia length in control and *EML1*-deficient cortical progenitors (* marks statistical significance in relation to Control 1, # in relation to Control 2, three biological replicates, four areas per sample, significance based on Kruskal–Wallis test and Dunn’s *post hoc* test, ****/###*P* = 0.0001).
- F Electron microscopy of primary cilia derived from control or *EML1*-deficient cortical progenitors in DMSO control or following EpothiloneD (EpoD) exposure (blue arrow: basal body, yellow arrow: appendages, and red arrow: ciliary pockets).
- G Quantification of primary cilia length in control and *EML1*-deficient cortical progenitors with/without EpoD exposure. Three biological replicates, four areas per sample, significance based on two-way ANOVA, and Sidak’s multiple comparisons *post hoc* test, *P* = 0.0213.

Data information: Data in graphs are represented as means ± SD. Scheme in C was designed using biorender.com. Scale bars: (A) 50 μm; (C) 5 μm; and (F) 0.5 μm. Source data are available online for this figure.

cultures upon EpoD treatment, we found a clearly improved primary cilia structure and a significant rescue of the primary cilia length in *EML1*-deficient EpoD-treated conditions compared to DMSO controls (Figs 2F and G, and EV2B). Our data confirm that *EML1*-deficiency leads to perturbed spindle orientation and primary cilia, which might directly impact aRG cell division mode and delamination resulting in ectopic progenitor cell localization.

Single-cell RNA sequencing (scRNAseq) and immunohistochemical analyses identify a perturbed progenitor cell population in *EML1*-deficient organoids

To further investigate the cellular identity of the ectopically located cells in *EML1*-deficient cerebral organoids, we performed scRNAseq on *EML1*-heKO 1 and respective isogenic control organoids (pooled dissected areas from nine organoids each, three independent batches, and day 33 ± 2; schematic overview Fig EV3A). We identified different cell populations including RG cells (RG1), RG cells transitioning to bRG cells (RG to bRG), RG cells transitioning to neurons (RG2), intermediate progenitors (IP), and young neurons (YN) based on known marker genes (Pollen *et al*, 2015; Liu *et al*, 2017; Nowakowski *et al*, 2017; Velasco *et al*, 2019; Fan *et al*, 2020) (Figs 3A and EV3B). In control organoids we detected expression of *EML1* in progenitor cells (Fig EV3C), an expression pattern

consistent with that found during early mouse and human brain development (Kielar *et al*, 2014; Nowakowski *et al*, 2017; Loo *et al*, 2019). We also observed the presence of a recently described mesenchymal-like cell cluster (MLC) (Eze *et al*, 2021) (Figs 3A and EV3B). As the function and role of these cells in cortical development is unclear, we excluded them from further analyses. When comparing the cell type composition between *EML1*-heKO and isogenic control-derived organoids, we found a clear decrease of 22.5% in RG1 cells and a striking increase of 23.4% in the abundance of RG to bRG cells in the *EML1*-heKO condition, while only minor variations in the other cell clusters were observed (Fig 3B). We further investigated molecular characteristics of the *EML1*-heKO-derived RG to bRG cluster compared to control. Here, we found a set of differentially expressed genes in the *EML1*-heKO. When further investigating these genes, we identified a clear upregulation of ECM and bRG markers (Pollen *et al*, 2015; Liu *et al*, 2017) in *EML1*-heKO-derived samples (Fig EV3D). The ECM genes *COL1A2*, *COL3A1*, and *LUM*, which are associated with human cerebral cortex expansion and folding (Fietz *et al*, 2012; Long *et al*, 2018), were found among the significantly upregulated genes in the *EML1*-heKO (Figs 3C and EV3D). Notably, a decrease in the expression of ECM genes including *COL1A2* was connected to reduced brain convolutions as found in lissencephaly (Karzbrun *et al*, 2018). It is tempting to speculate that an increase in these ECM genes in the *EML1*-heKO might play a role in the development of the

Figure 3. ScRNA-seq reveals cellular identity of ectopic cells in *EML1*-heKO cerebral organoids.

- A scRNA-seq of 2,335 control and 3,358 *EML1*-heKO cells (three pooled independent batches and three organoids each). Cells shown in UMAP plot and colored by annotated cell type.
- B Comparison of cell type composition between control and *EML1*-heKO. Numbers indicate percentage of total cells belonging to the respective cell type.
- C Normalized expression values of *COL1A2*, *COL3A1*, *LUM*, and *MEIS2* per cell type (three pooled batches and three organoids each).
- D Gene ontology (GO) term analysis of RG to bRG cells in control and *EML1*-heKO shows percentage of counts belonging to the set of genes associated with the respective GO term (three pooled batches and three organoids each).
- E Control- and *EML1*-heKO-derived cerebral organoid stained for *COL1A2* and *MEIS2*. VZ areas are encircled, and squares indicate areas enlarged in F.
- F Control- and *EML1*-heKO-derived cerebral organoid stained for *COL1A2*, *MEIS2*, and MAPT.
- G Representative images showing EGFP control and EGFP-*EML1*-heKO hybrid cerebral organoid stained for EGFP, FAM107A, and NCAD. Yellow dotted lines indicate morphology of EGFP⁺ cells (4 independent batches each, 3 organoids per batch, at least 30 ectopic rosettes in total).

Data information: RG1: radial glia1, RG to bRG: radial glia to basal radial glia, RG2: radial glia to young neurons, IP, intermediate progenitors; YN, young neurons; MLC, mesenchymal-like cells. (C and D) Asterisks indicate Bonferroni corrected *P*-values. Wilcoxon rank sum test: ***< 0.001, *< 0.05, ns, not significant. Scale bars: (E) 50 μm; (F) 10 μm; and (G) 50 μm, enlarged 10 μm.

Source data are available online for this figure.

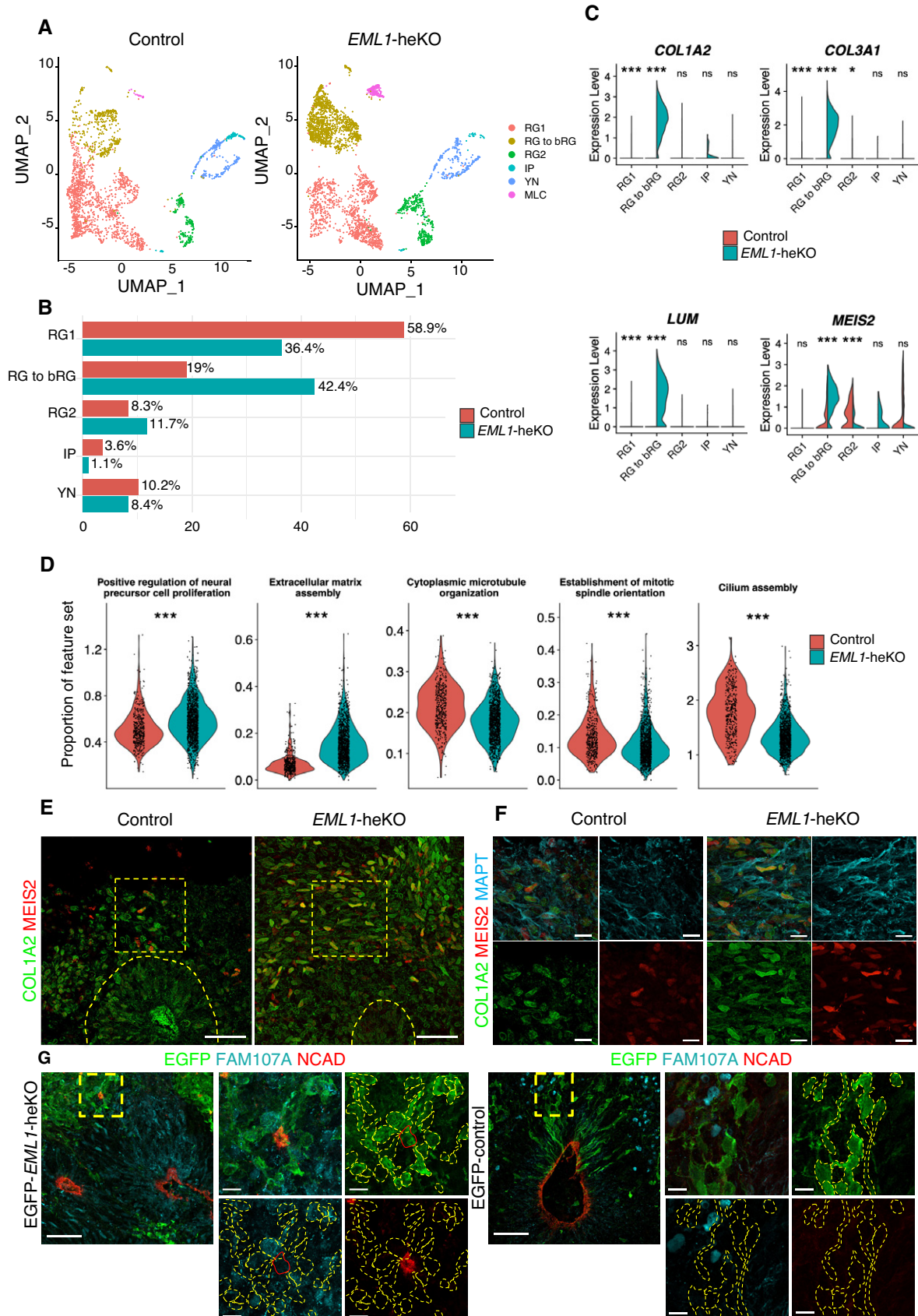


Figure 3.

polymicrogyria-like cortex and megalencephaly observed in patient MRIs (Oegema *et al*, 2019). We also found that the proneurogenic gene *MEIS2* was significantly enriched in this cluster in the *EML1*-heKO (Fig 3C). GO term analyses reveal significant alterations in positive regulation of neural precursor cell proliferation, ECM assembly, cytoplasmic microtubule organization, establishment of mitotic spindle orientation, and cilium assembly in the *EML1*-heKO RG to bRG cell cluster compared to control (Fig 3D). When performing immunocytochemical analyses on *EML1*-heKO and isogenic control organoids (day 33 ± 2) we found in the control a few COL1A2 and MEIS2⁺ cells in the CP area, some of which co-stain for MAPT, whereas *EML1*-heKO samples exhibit a broader co-expression of COL1A2 and MEIS2 with hardly any overlap with MAPT within the ectopic cell population (Figs 3E and F, and EV3E and F, day 33 ± 2). To further delineate the nature of the ectopic progenitor cells, we applied our hybrid organoids. This system allows to decipher the morphology of the cells within the ectopic rosettes as well as their marker expression. When investigating EGFP-*EML1*-heKO hybrid organoids at day 30 ± 2, we found EGFP⁺ cells organized into ectopic rosettes, which were marked by accumulation of NCAD in their centers (Fig 3G). The EGFP⁺ cells found around the NCAD centers exhibit different morphologies. Most of the cells do not show a RG-like elongated organization with an apical and/or basal process but rather perturbed morphologies (Fig 3G). Some of the ectopic cells stain positive for the bRG marker FAM107A (Fig 3G). Individual EGFP/FAM107A double-positive ectopic cells contact the centers of the rosettes suggesting an apical domain enriched in NCAD, very unusual for bRG cells during normal brain development (Fig 3G, (Martínez-Martínez *et al*, 2016)). In control hybrids, the majority of the EGFP⁺ cells found at a basal location to the VZ areas exhibited a radial morphology with an apical and/or basal process. Taken together, our data suggest that the ectopic progenitors in the *EML1*-heKO are composed of a perturbed progenitor population, which does not exist as such in control organoids or is very rare and is most likely

not reflecting a cell population present during normal human brain development.

Deregulated YAP signaling in *EML1*-deficient organoids drives ectopic cell expansion

To further dissect progenitor cell behavior that may be responsible for the large numbers of ectopic localized progenitor cells, we examined cell proliferation (day 20 ± 2). We found a significant increase in mitotic cells (labeled with p-VIM) located at the basal side of the VZ areas in all *EML1*-deficient organoids compared to the controls (Figs 4A and EV4A). No clear change in cell mitosis at the VZ surface was observed between the different conditions (Fig EV4B). We also found that the basally located mitotic cells in the *EML1*-deficient organoids exhibit an increase in cell cycle re-entry (quantified by BrdU⁺ KI67⁺ cells) compared to the control (Figs 4B and EV4C). In addition, GO-term analyses confirmed an enhanced positive regulation of cell proliferation in the RG to bRG cell cluster (Fig 3D). The distinct increase in mitotic cell behavior outside the VZ areas raises the intriguing question about the underlying mechanisms. Recent data from mice suggest that premature cortical progenitor delamination, ectopic rosette formation, periventricular neuronal heterotopia, and megalencephaly might result from deregulation of the Hippo signaling pathway (Cappello *et al*, 2013; Liu *et al*, 2018; O'Neill *et al*, 2018; Saito *et al*, 2018; Najas *et al*, 2020)—a conserved signaling pathway that controls cell proliferation and tissue development (Camargo *et al*, 2007; Zhao *et al*, 2011). To assess whether YAP1, a major downstream effector of the Hippo pathway (Sahu & Mondal, 2021), is altered in *EML1*-deficient cerebral organoids, we investigated YAP1 expression in our scRNAseq data. We found a significant upregulation of YAP1 in the *EML1*-KO RG to bRG cell cluster compared to control (Figs 4C and EV4D). We further analyzed expression of the YAP1 interaction partner TEAD2 (Mukhtar *et al*, 2020) and downstream target genes *CCND3* and *CYR61* and found that they exhibit significantly increased expression

Figure 4. YAP signaling drives ectopic progenitor cell expansion in *EML1*-deficient organoids.

- A Quantification of mitotic cells located at the basal side of VZ areas in control and *EML1*-deficient conditions (three batches and three organoids analyzed per batch).
- B Quantification of BrdU⁺ KI67⁺ cells located at the basal side of VZ areas in control and *EML1*-deficient conditions (three batches and three organoids analyzed per batch).
- C Normalized expression of YAP1, TEAD2, CCND3, and CYR61 in RG to bRG cells. Separate violins show expression in control and *EML1*-heKO. Asterisks indicate Bonferroni corrected *P*-values. Percentages indicate amount of cells in each group expressing the respective gene (three pooled batches and three organoids each).
- D, E Immunofluorescence staining for (D) p-VIM and YAP1 or (E) Pax6 and YAP1 in control- and *EML1*-heKO-derived organoids (day 20 ± 2, squares indicate areas enlarged in adjacent part of the panel, respectively).
- F Quantification of basally located p-Vim⁺ cells with nuclear YAP1 signal per VZ area in control- and *EML1*-heKO-derived organoids (three batches and three organoids analyzed per batch).
- G Quantification of PAX6⁺ cells with nuclear YAP1 signal per VZ area in control- and *EML1*-heKO-derived organoids (three batches and three organoids analyzed per batch).
- H Immunofluorescence staining for p-Vim in *EML1*-heKO- and control-derived organoids in DMSO-, Verteporfin-, or Fluvastatin-treated conditions, counterstained with DAPI. Dotted line indicates VZ areas.
- I Quantification of p-VIM⁺ cells located at the basal side of VZ areas in control- or *EML1*-heKO-derived organoids under DMSO-, Verteporfin-, or Fluvastatin-treated condition (three batches and three organoids analyzed per batch).
- J Quantification of ectopic neural rosettes per VZ area in *EML1*-heKO-derived organoids in DMSO-, Verteporfin-, or Fluvastatin-treated conditions (three batches and three organoids analyzed per batch).

Data information: Data in graphs are represented as means ± SD. Significance based on Kruskal–Wallis test (A–B, F, G, J), or two-way ANOVA (on log₁₀ normalized data) (I) or Wilcoxon rank sum test (C). Dunn's *post hoc* (A, F–G, J) or Tukey *post hoc* (I) test for multiple comparisons was performed to define statistical differences between genotypes. *P*-values: *** < 0.001, ** < 0.01, * < 0.05. Scale bars: (D and E) 50 μm, enlarged 10 μm; (H) 50 μm.

Source data are available online for this figure.

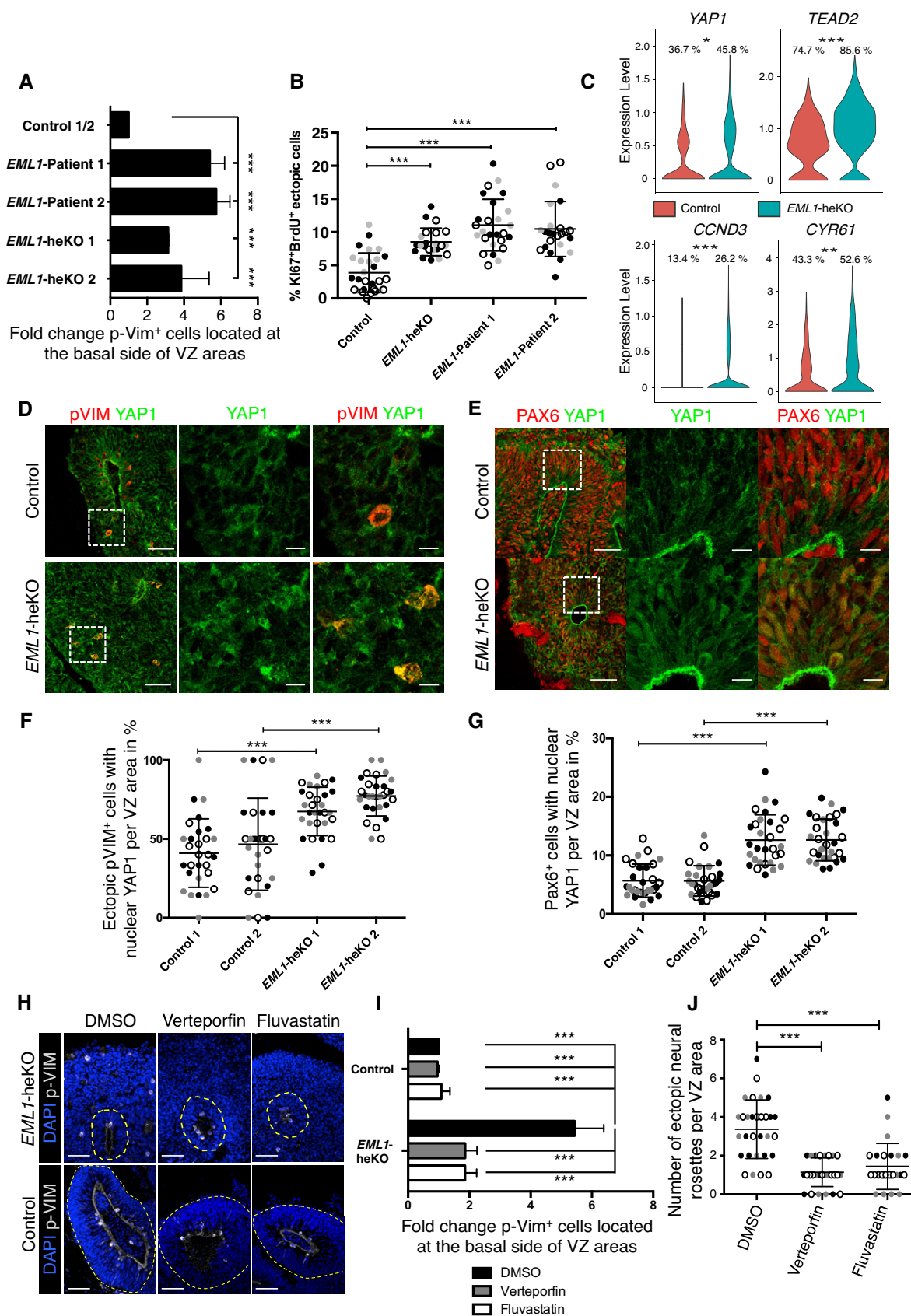


Figure 4.

levels in the RG to bRG cluster of the *EML1*-KO (Figs 4C and EV4D). To further test whether YAP1 signaling is indeed associated with the massive expansion of the ectopic progenitor cells, we stained control and *EML1*-heKO sections with an antibody against YAP1 and p-VIM (day 20 ± 2). Here, we found significantly more basally located p-VIM-positive cells exhibiting nuclear YAP1, suggesting active YAP1, in *EML1*-heKO-derived organoids compared to the isogenic control (Fig 4D and F). We also observed a significant increase in nuclear YAP1 in PAX6⁺ cells within the VZ areas in the *EML1*-heKO compared to controls (Fig 4E and G). Of note, most of the nuclear YAP1 PAX6 co-expressing cells were located in distal positions to the VZ surface (Fig 4E). To further determine the functional role of YAP1 in driving defective RG cell behavior and cortical malformation, we pharmacologically inhibited YAP1 function using Verteporfin (Kostic *et al*, 2019) or its nuclear translocation using Fluvastatin (Oku *et al*, 2015). Decrease in nuclear YAP1 upon Fluvastatin treatment was confirmed by immunohistochemistry (Fig EV4E). When assessing progenitor cell proliferation, we found a significant decrease in mitotic cells at the basal side of the VZ areas in Verteporfin- and Fluvastatin-treated *EML1*-heKO organoids. No difference in ab-ventricular cell mitosis could be observed in control organoids upon Verteporfin or Fluvastatin treatment (Fig 4H and I). In addition, pharmacological inhibition of YAP1 significantly reduced the numbers of ectopic neural rosettes in *EML1*-heKO organoids (Figs 4J and EV4F). YAP1 was reported to contribute to the evolutionary expansion of the neocortex by promoting bRG cell proliferation (Kostic *et al*, 2019). It is tempting to speculate that YAP1 is activated in the ectopic progenitor cells due to their basal location in the tissue, by that representing an indirect effect of *EML1* deficiency. Of note, additional signaling pathways might be impacted by *EML1* deficiency and it would be interesting to further investigate them in the future.

Concluding remarks

Using a human *in vitro* model, we identified for the first time that deficiency in *EML1* leads to the formation of ectopic neural rosettes and occurrence of perturbed progenitor cells, which show increased ECM production and YAP1-mediated expansion. In addition, we confirmed a role of *EML1* in primary cilia formation and progenitor cell proliferation. Although this study shows the formation of ectopic cells (heterotopia) and allowed us to decipher new underlying pathomechanisms in *EML1*-deficient cerebral organoids, which were not yet identified in *Eml1*-mouse models, the developmental stage of the model used does not fully enable us to investigate the entire scope of MCD in humans caused by *EML1* impairment. For instance, the direct correlation between perturbed *EML1*-derived progenitor cells and the observed polymicrogyria-like cortex and megalencephaly in *EML1* patients needs to be further investigated. It is also of note that the organoid system is prone to heterogeneity and even though we could reproduce major findings in two *EML1* patient-derived and two *EML1*-heKO lines, key experiments should be repeated in additional iPSC lines to ensure full reproducibility. Nevertheless, our human *in vitro* approach allowed insight into so far not described pathological features and pathomechanisms of early stages of heterotopia formation.

Material and Methods

Generation of human iPSC cells

Skin fibroblasts were obtained from the Coriell Biorepository (Control 1, 2-year-old female, catalog ID GM00969), from a healthy donor (Control 2, 44-year-old healthy female derived with given informed consent within the collaborative research center project SFB636 B7 (ID number B7_028#4)) and from two patients harboring mutations in the *EML1* gene (Patient 1, P135, 14 years male; Patient 2, 3489, newborn (8 days) male), both with given informed consent and obtained according to the guidelines of the local institutional review boards (IRBs APHP-Délégation Interrégionale à la Recherche Clinique, Paris and Erasmus Medical Center, Rotterdam). Research on human cells was approved by the French Ministry of Health (L.1243.3, DC-2015-2559). Patient 1 carries a compound heterozygous *EML1* mutation. An A c.481C>T nucleotide mutation in exon 5, changing an arginine residue (Arg138) to a stop codon, and a c.796A>G mutation in exon 8, changing a threonine into an alanine residue, leading to an impaired association of *EML1* with microtubules. Patient 2 carries a c.673T>C mutation—W225R, in which a hydrophobic nonpolar residue changed to highly basic hydrophilic residue—this residue can be found deep in the beta propeller structure where the HELP domain is present (Kielar *et al*, 2014; Richards *et al*, 2014). Fibroblasts were reprogrammed by non-integrative delivery of OCT4, SOX2, KLF4, and c-MYC using Sendai virus (SeV) vectors (CytoTune-iPS 2.1 Sendai Reprogramming Kit, Thermo Fisher (Ban *et al*, 2011); Ethics Committee II of Heidelberg University approval no. 2009-350N-MA for hiPSC generation). Pluripotent stem cells were validated as described in Iefremova *et al* (2017). iPSCs were cultured as colonies in Essential 8 (E8) medium on Geltrex-coated (GT, Thermo Fisher Scientific) cell culture plates with daily medium change. Cells were passaged using EDTA (Thermo Fisher Scientific) and seeded in a 1:3 to 1:10 ratio. Following passaging, medium was supplemented with 5 μM Y-27632 (Cell Guidance Systems) to promote cell survival. All human iPSC cell lines were regularly checked and confirmed negative for mycoplasma. Reagents and resources used in this study can be seen in Table 1.

Generation and validation of *EML1*-heKO lines

EML1-heKO lines were generated using CRISPR/Cas9 and homology-directed repair (HDR) (Santa Cruz). Successful site-specific double-strand break followed by integration of the HDR sequence leads to the disruption of the *EML1* gene and the integration of a puromycin selection cassette. In brief, 1 million iPSC cells derived from either control 1 or control 2 were transfected with three different gRNAs (1 μg in total) directed against early exons of the *EML1* gene (Exons 2 and 5) alongside the respective HDR plasmids using the NucleofectorTM2b (Lonza) and the Cell Line Nucleofector[®] Kit V (Lonza) according to the manufacturer's protocol. Following nucleofection, cells were plated on GT-coated cell culture plates in E8 medium supplemented with 5 μM Y-27632. Puromycin (1 μg/ml, Merck Milipore) selection was initiated 48 h following nucleofection. Clones were manually picked 7–12 days following nucleofection into GT-coated 48-well cell culture plates. Integration of the HDR cassette was validated on genomic DNA by PCR. PCR primers were designed to recognize the *EML1* wild-type allele

Table 1. Reagents and resources used in this study.

Reagent or Resource	Vendor	Identifier
A83-01	Biomol	Cay9001799
B27-Supplement	Thermo Fisher Scientific	17504044
BCA Protein Assay Kit	Thermo Fisher Scientific	23225
Blasticidin S Hydrochlorid	Carl Roth	CP14.2
Boric acid	Thermo Fisher Scientific	B0394
BrdU	BD-Bioscience	550891
BSA	Sigma Aldrich	A3294
cAMP	Sigma Aldrich	D0627
Chromium Single Cell 3' Library & Gel Bead Kit v2	10xGenomics	PN-120267
DAPI	Biolegend	422801
DMEM/F12	Thermo Fisher Scientific	11320074
DMEM/F-12 with Glutamin and HEPES	Thermo Fisher Scientific	11330-057
DNase	Sigma Aldrich	AMPD1-1KT
PBS	Sigma Aldrich	D8537
EDTA	Thermo Fisher Scientific	15575020
EML1 CRISPR/Cas9 KO Plasmid (h)	Santa Cruz	sc-406445
EML1 HDR Plasmid (h)	Santa Cruz	sc-406445-HDR
EpothiloneD	Abcam	ab143616
Epoxy resin	PolyScience	EPON218
Extractme Genomic DNA Kit	7Bioscience	EM13
Fetal Bovine Serum (FBS)	Thermo Fisher Scientific	10270106
FGF-2 (154)	Cell Guidance Systems	GFH146
Fluvastatin	Sigma Aldrich	SML0038
Geltrex, hESC-Qualified	Thermo Fisher Scientific	A1413302
Glucose	Carl Roth	HN06.2
GlutaMAX	Thermo Fisher Scientific	35050038
Glutaraldehyde	Sigma Aldrich	G5882
HCL	Thermo Fisher Scientific	15538334
Heparin	Sigma Aldrich	H3149
Insulin	Sigma Aldrich	91077C
iScript cDNA synthesis kit	Bio-Rad	1708890
KnockOut Serum Replacement (KOSR)	Thermo Fisher Scientific	10828028
LAAP	Sigma Aldrich	A8960
L-cysteine	Sigma Aldrich	168149
LDN-193189	Cell Guidance Systems	SM23
Mowiol 4-88	Carl Roth	0713.1

Table 1 (continued)

Reagent or Resource	Vendor	Identifier
N2-Supplement	Thermo Fisher Scientific	17502048
Natriumselenit	Sigma Aldrich	S5261
NEAA	Thermo Fisher Scientific	11140035
Papain	Sigma Aldrich	P3125
Paraformaldehyd (PFA)	Sigma Aldrich	P6148
Penicillin/Streptomycin	Thermo Fisher Scientific	15140122
peqGOLD TriFast	VWR	30-2010
Pierce™ Protease Inhibitor	Thermo Fisher Scientific	A32955
Pluronic F-127	Sigma Aldrich	P2443
Puromycin	Merck Millipore	540222
SDS	Carl Roth	CN30.1
Sendai Reprogramming Kit (CytoTune-iPS 2.1)	Thermo Fisher Scientific	A16517
Taq Polymerase	Biozym	331610
TGFβ1	Cell Guidance Systems	GFH39
Transferrin	Sigma Aldrich	T3705
Triton X-100	Merck Millipore	108603
TrypLE Express	Thermo Fisher Scientific	12605-028
Verteporfin	Sigma Aldrich	SML0534
XAV939	Cell Guidance Systems	SM38
Y-27632	Cell Guidance Systems	SM02

or the integration of the puromycin cassette. Of note: only heterozygous *EML1*-(he)KO iPSC clones could be expanded, stored, and further differentiated into cerebral organoids.

Generation of cerebral organoids

Cerebral organoids were generated as described with slight adaptations (Iefremova *et al*, 2017; Krefft *et al*, 2018). In brief, U-bottom 96-well plates were coated with 5% Pluronic F-127 (Sigma Aldrich) in phosphate buffered saline (PBS) for 15 min to create low attachment wells. iPSC cell colonies were dissociated using TrypLE Express (Thermo Fisher Scientific) and 6,000 cells were plated per low attachment well in 150 μl E8 medium supplemented with 50 μM Y-27632. Medium was changed every other day. At day 5, medium was changed to neural induction medium (Table 2). Medium was changed every other day. On days 9–11, when translucent neural ectoderm was visible, organoids were embedded in a 3:2 ratio of GT to neural induction medium and further cultured in Pluronic F-127-coated 6 cm dishes in neural differentiation medium (Table 3) under continuous agitation at 70 rpm on an orbital shaker (Infors Celltron HD) with a medium change every 3 to 4 days. When indicated, organoids were exposed to 100 nM Verteporfin (Sigma

Table 2. Neural induction medium.

Component	Final conc.
DMEM/F12	93.3%
N2 supplement	0.5% (v/v)
B27 supplement	1%
cAMP	300 ng/ml
LDN-193189	0.2 mM
A83-01	0.5 mM
XAV939	2 μ M
GlutaMAX	1% (v/v)
NEAA	1% (v/v)
D-Glucose	4.44 mM
Heparin	10 μ g/ml
KOSR	2% (v/v)
Penicillin/Streptomycin	1% (v/v)

Table 3. Neural differentiation medium.

Component	Final conc.
DMEM/F12	93.3%
N2 supplement	0.5% (v/v)
B27 supplement	1%
cAMP	300 ng/ml
GlutaMAX	1% (v/v)
NEAA	1% (v/v)
D-Glucose	4.44 mM
Insulin	2.5 μ g/ml
KOSR	2% (v/v)
Penicillin/Streptomycin	1% (v/v)

Aldrich) or 300 nM Fluvastatin (Sigma Aldrich) for 96 h from day 16 onwards with daily medium changes.

Generation of hybrid organoids

EGFP-labeled iPS cells (*EML1*-heKO and isogenic control) were generated using a lentiviral construct expressing EGFP under the PGK promoter as well as a blasticidin resistance cassette (pLentiPGK-EGFP-SV40-blasticidin (Koch *et al.*, 2006)). Forty-eight hours post-transfection, iPS cells were cultured for at least 2 weeks using E8 medium supplemented with 10 μ g/ml blasticidin (Carl Roth). Homogeneous EGFP expression was validated by visual monitoring using epifluorescence microscopy. Hybrid organoids were generated by mixing either control-EGFP- or *EML1*-heKO-EGFP-derived iPS cells with control iPS cells in a 1:1,000 ratio before organoid generation.

BrdU labeling of cerebral organoids

For 5-bromo-2'-deoxyuridine (BrdU) labeling, day 30 \pm 2 cerebral organoids were incubated for 2 h in medium containing 10 μ M BrdU (BD Bioscience). After 2 h of incubation, cerebral organoids

were washed three times with fresh medium and transferred into a new 6 cm culture dish. Following 24 h, cultivation time cerebral organoids were fixed and further processed for immunohistochemistry.

Generation of iPS cell-derived cortical progenitors

Differentiation of iPS cells into cortical progenitors was performed as described with slight adaptations (Shi *et al.*, 2012; Iefremova *et al.*, 2017; Uzquiano *et al.*, 2019). In brief, iPS cell colonies cultured in E8 medium were dissociated using TrypLE (Thermo Fisher Scientific) and seeded as single cells onto GT-coated cell culture plates in E8 medium supplemented with 5 μ M Y-27632. Once the cell culture reached 98% confluence, neural induction was initiated by changing the culture medium to neural induction medium containing DMEM/F12 (Thermo Fisher Scientific), 0.5% N2 supplement, 1% B27 supplement, (Thermo Fisher Scientific), cAMP (300 ng/ml, Sigma Aldrich), LDN-193189 (0.2 mM, Cell Guidance Systems), A83-01 (0.5 mM, Biomol), XAV939 (2 μ M, Cell Guidance Systems), 1% GlutaMAX (Thermo Fisher Scientific), 1% NEAA (Thermo Fisher Scientific), and 4.44 mM Glucose (Carl Roth). Cells were maintained in this medium for 8–11 days, collected by dissociation with TrypLE and replated in neural differentiation media containing DMEM/F12, 0.5% N2 supplement, 1% B27 supplement, and cAMP (300 ng/ml) on GT-coated cell culture plates. Cells were split in a 1:2 ratio when cultures reached 100% confluence using TrypLE. Electron microscopy analyses were performed on cortical progenitors passaged twice. When indicated, 0.5 nM EpothiloneD (EpoD, abcam) was added to the medium for 72 h with one medium change after 48 h before cells were fixed and analyzed or harvested for Western blot analysis.

Electron microscopy of neural progenitor cells

Samples were processed and imaged as previously described in Uzquiano *et al.* (2019). Briefly, cells were fixed for 1 h in phosphate buffer (PB), 0.1 M buffer containing 4% paraformaldehyde (PFA, Sigma Aldrich), and 2.5% glutaraldehyde (Sigma Aldrich) at 4°C. Following fixation, cells were postfixed in 2% osmium tetroxide diluted in 0.2 M Palade buffer. After osmication, cells were dehydrated in a series of ethanol baths and flat embedded in epoxy resin (EPON 812, Polysciences). After resin polymerization, small pieces were dissected from flat-embedded cultures, mounted in plastic stubs and sectioned. Ultrathin sections (70 nm) were stained with uranyl acetate and lead citrate. Sections were examined in a Philips CM100 electron microscope. Digital images were obtained with a CCD camera (Gatan Orius).

Immunofluorescence and specific antibody information

Cells were washed twice with PBS, fixed for 10 min with 4% PFA, and washed again twice with PBS and used either directly for immunostaining or stored at 4°C. Organoids were fixed, embedded, and cryo-sectioned into 20 μ m sections as described previously (Iefremova *et al.*, 2017; Krefft *et al.*, 2018). For detection of the pluripotency-associated markers, TRA-1-60, TRA-1-81, and SSEA-3 samples were incubated with primary antibodies at room temperature for 4 h, washed three times, incubated with secondary antibody for 45 min, counterstained with DAPI (Biolegend), and mounted with Mowiol 4-88 mounting solution (Carl Roth). For detection of BrdU and Ki67,

slices were permeabilized using 0.5% Triton X-100 in PBS for 30 min, washed with PBS, treated with 2 N HCl (Thermo Fisher Scientific) for 10 min, and washed twice with PBS. Then, slices were treated with 0.1 M boric acid (Thermo Fisher Scientific) for 10 min and washed three times with PBS. Slices were then blocked with 10% fetal bovine serum and 0.1% Triton X-100 in PBS for 1 h at room temperature and subsequently stained overnight in blocking solution at 4°C with antibodies against BrdU and Ki67. On the next day, slices were washed three times with PBS and secondary antibodies were applied in blocking solution for 1 h at room temperature, counterstained with DAPI, and mounted with Mowiol. For all other antibodies, cells or organoid sections were blocked and permeabilized in 10% fetal bovine serum (Thermo Fisher Scientific) in PBS with 0.3% Triton X-100 for 1 h at room temperature (RT), incubated with primary antibodies for 16 h at 4°C, washed three times with PBS, incubated with secondary antibodies for 1 h, counterstained with DAPI, and mounted with Mowiol. Images were acquired with either the confocal microscope Leica TCS SP5II or the fluorescence microscope Leica DM6 B microscope and processed using the software Leica Application Suite AF, Leica Application Suite X, as well as ImageJ.

Primary and secondary antibodies and dilutions used in this study can be seen in Tables 4 and 5. Software and algorithms used for analysis can be seen in Table 6.

Immunoblot and specific antibody information

Cells were washed twice with ice-cold PBS, scraped off into PBS, and collected via centrifugation. Cell pellets were lysed in RIPA buffer (150 mM NaCl, 0.2% SDS (Carl Roth), 0.2% Triton X-100 (Merck Millipore), 25 mM EDTA, 50 mM Tris-HCl, pH 7.4) containing Pierce™ protease inhibitor (Thermo Fisher Scientific) and Pierce™ phosphatase inhibitor (Thermo Fisher Scientific) for 1 h on ice. Genomic DNA was sheared by sonication. Subsequently, cell debris was precipitated by centrifugation at 16,000 rcf for 15 min at 4°C. Protein concentration of cleared cell lysates was determined using the BCA protein assay kit (Thermo Fisher Scientific). For immunoblotting, 25 µg of protein was boiled in 6× SDS sample buffer for 5 min at 95°C. Lysates were resolved on 10% gels and transferred onto 0.2 µm nitrocellulose membranes by semi-dry blotting. Nitrocellulose membranes were blocked in 5% BSA in TBST for 1 h at RT and subsequently incubated overnight with primary antibody in blocking solution at 4°C. The next day, membranes were washed three times with TBST, incubated with IR-dye-conjugated secondary antibodies (DyLight™, Cell Signaling Technology) diluted 1:15,000 in TBST for 1 h at room temperature. Subsequently, membranes were washed three times before visualization of target proteins using an Odyssey IR imaging system (LI-COR Biosciences). Primary antibodies and concentrations were as follows: Acetylated α -tubulin (AC-TUB) (Cell Signaling Technology, 1:1,000) and β -Actin (Cell Signaling Technology, 1:15,000). Of note: due to the lack of a reliable EML1 antibody, we were not able to include data on EML1 protein levels.

Single-cell RNA sequencing experiments

Organoids at day 33 \pm 2 were microdissected to enrich for cortical areas. The dissected tissue was dissociated by incubating in papain (Sigma Aldrich) solution containing papain buffer (1 mM L-cysteine and 0,5 mM EDTA in Earle's balanced salt solution), 20 units

Table 4. Antibodies used in this study.

Reagent or Resource	Vendor	Identifier
Antibodies IF		
AFP	Hözel	Cat# 12177-MM27
ARL13B	Antibodies Incorporated	Cat# 75-287, RRID: AB_2341543
Anti-BrdU	BD-Biosciences	Cat# 347580, RRID: AB_10015219
COL1A2	Abcam	Cat# ab96723, RRID: AB_10679394
FAM107A	Sigma Aldrich	HPA055888
Anti-GFP	Aves Labs	Cat# GFP-1020, RRID: AB_10000240
Ki67	Cell Signaling	Cat# 9129 RRID: AB_2687446
MAPT	Synaptic Systems	Cat# 314 004, RRID: AB_1547385
MEIS2	Sigma Aldrich	Cat# WH0004212M1, RRID: AB_1842419
N-cadherin	BD-Bioscience	Cat# 610921, RRID: AB_398236
PAX6	Biologend	Cat# 901301, RRID: AB_2565003
p-Vimentin	MBL	Cat# D076-3, RRID: AB_592963
SMA	abcam	Cat# ab5694, RRID: AB_2223021
TPX2	Novus Biologicals	Cat# NB500-179, RRID: AB_10002747
TRA-1-60	Merck Millipore	Cat# MAB4360, RRID: AB_2119183
TRA-1-81	Merck Millipore	Cat# MAB4381, RRID: AB_177638
TUBB3	Biologend	Cat# 802001, RRID: AB_2564645
SSEA3	abcam	Cat# ab16286, RRID: AB_882700
YAP1	Cell Signaling	Cat# 14074, RRID: AB_2650491
Alexa Fluor 568 -Goat anti-mouse IgG (H + L)	Thermo Fisher Scientific	Cat# A-11004, RRID: AB_2534072
Alexa Fluor 488 -Goat anti-Rabbit IgG (H + L)	Thermo Fisher Scientific	Cat# A-11008, RRID: AB_143165
Alexa Fluor 555 -Goat anti-Rabbit IgG (H + L)	Thermo Fisher Scientific	Cat# A-21428, RRID: AB_2535849
Alexa Fluor 647 -Goat anti-Guinea Pig IgG (H + L)	Thermo Fisher Scientific	Cat# A-21450, RRID: AB_2735091
Alexa Fluor 488 -Goat anti-Chicken IgY (H + L)	Thermo Fisher Scientific	Cat# A-11039, RRID: AB_2534096
Antibodies immunoblot:		
Acetylated α -tubulin (AC-TUB)	Cell Signaling Technology	5335, RRID: AB_10544694
β -Actin	Cell Signaling Technology	3700, RRID: AB_2242334

Table 4 (continued)

Reagent or Resource	Vendor	Identifier
Anti-mouse IgG (H + L) (DyLight 680 Conjugate)	Cell Signaling Technology	5470, RRID: AB_10696895
Anti-rabbit IgG (H + L) (DyLight 800 4X PEG Conjugate)	Cell Signaling Technology	5151, RRID: AB_10697505

papain, and 10 µg/ml of DNase (Sigma Aldrich) for 20 min at 37°C. Following incubation, excessive papain solution was removed, 3 ml organoid differentiation medium was added, and samples were mechanically dissociated using wide-bore 1,000 µl pipette tips coated with 1% bovine serum albumin (BSA) in PBS. The cell suspension was centrifuged at 400 g for 4 min at 4°C. The supernatant was removed, the cell pellet was resuspended in 1 ml ice-cold PBS + 0.04% BSA, and filtered through a 30 µm cell strainer. Counting and viability were assessed using Trypan blue staining (Countess automatic cell counter, Thermo Fisher Scientific). Single cell library preparation was performed using the 10x Genomics Chromium platform according to the 10x Genomics Chromium Single Cell 3' Library & Gel Bead Kit v2 chemistry user guide (10x Genomics).

The prepared cDNA libraries were processed by the High Throughput Sequencing Unit of the Genomics & Proteomics Core Facility of the German Cancer Research Center (DKFZ). The libraries were sequenced on two lanes on the Illumina HiSeq 4K platform with a protocol specific for 10x scRNA libraries (paired-end 26 + 74).

Fastq files were parsed to cellranger (10x Genomics) count in order to generate a count matrix. FastQC was used for general sequencing quality control (Andrews, 2015). If not stated otherwise, data analysis was performed using the Seurat (v3.2.2) package in R (Stuart *et al*, 2019). Count matrix was filtered with following parameters: Any feature that was expressed in less than three cells was removed from the analysis. For the control sample, any cell with < 2,000 expressed features, more than 10% mitochondrial genes expressed, or less than 5,000 total UMI counts was removed from further analysis. For the *EML1*-heKO sample, any cell with < 1,500 expressed features, more than 10% mitochondrial genes expressed, or < 3,000 total UMI counts was removed from further analysis. The data were normalized using SCTransform. Dimensional reduction was performed using UMAP with dims = 1:30. Shared nearest-neighbor graph was constructed with dims = 1:30. Clusters were generated with resolution = 0.4. Cells were defined by interpreting expression of known marker genes. One group of cells that was defined as

Table 5. Primary antibodies and dilutions.

Antibodies	Vendor	Cat. No.	Raised against	Dilution
Primary antibodies				
AFP	Hözel	Cat# 12177-MM27	mouse	1:300
ARL13B	Antibodies Incorporated	Cat# 75-287	mouse	1:100
Anti-BrdU	BD-Biosciences	Cat# 347580	mouse	1:50
COL1A2	Abcam	Cat# ab96723	rabbit	1:300
FAM107A	Sigma Aldrich	Cat# HPA055888	rabbit	1:400
Anti-GFP	Aves Labs	Cat# GFP-1020	chicken	1:500
KI67	Cell Signaling	Cat# 9129	rabbit	1:500
MAPT	Synaptic Systems	Cat# 314 004	guinea pig	1:1,000
MEIS2	Sigma	Cat# WH0004212M1	mouse	1:200
N-cadherin	BD-Bioscience	Cat# 610921	mouse	1:500
PAX6	Biologend	Cat# 901301	rabbit	1:500
p-Vimentin	MBL	Cat# D076-3	mouse	1:1,000
SMA	abcam	Cat# ab5694	rabbit	1:300
TPX2	Novus Biologicals	Cat# NB500-179	rabbit	1:500
TRA-1-60	Merck Millipore	Cat# MAB4360	mouse	1:300
TRA-1-81	Merck Millipore	Cat# MAB4381	mouse	1:300
TUBB3	Biologend	Cat# 802001	rabbit	1:1,000
SSEA3	abcam	Cat# ab16286	rat	1:500
YAP1	Cell Signaling	Cat# 14074	rabbit	1:300
Secondary antibodies				
Alexa Fluor 568-Goat anti-mouse IgG (H + L)	Thermo Fisher Scientific	Cat# A-11004	goat anti-mouse	1:1,000
Alexa Fluor 488-Goat anti-Rabbit IgG (H + L)	Thermo Fisher Scientific	Cat# A-11008	goat anti-rabbit	1:1,000
Alexa Fluor 555-Goat anti-Rabbit IgG (H + L)	Thermo Fisher Scientific	Cat# A-21428	goat anti-rabbit	1:1,000
Alexa Fluor 647-Goat anti-Guinea Pig IgG (H + L)	Thermo Fisher Scientific	Cat# A-21450	goat anti-guinea	1:1,000
Alexa Fluor 488-Goat anti-Chicken IgY (H + L)	Thermo Fisher Scientific	Cat# A-11039	goat anti-chicken	1:1,000

Table 6. Software and algorithms used in this study.

Software and Algorithms	Source	Identifier
Cellranger v 3.0.1	10x Genomics	https://support.10xgenomics.com/single-cell-gene-expression/software/downloads/latest
Fiji software (ImageJ 1.52i)	Wayne Rasband, NIH, USA	Fiji, RRID:SCR_002285
ggplot2	Hadley (2016)	RRID:SCR_014601
Prism 6	GraphPad Prism version 6.0d	GraphPad Prism, RRID:SCR_002798
Seurat v3.0.0	Stuart et al (2019)	https://github.com/satijalab/seurat/releases/tag/v3.0.0
SPSS	https://www.ibm.com/	IBM SPSS statistics 25
R	R Core	https://www.r-project.org/

mesenchymal-like cells was removed for further analysis. Violin plots were generated with Seurat (Stuart et al, 2019) and ggplot2 (Hadley, 2016) and show normalized expression values. For GO violin plots, the genes that are collected in a GO term were retrieved from org.Hs.eg.db (org.Hs.eg.db: Genome wide annotation for Human. R package version 3.12.0.). For each GO term of interest, the expression per cell was calculated as proportion of feature set. For detailed information about the data analysis pipeline in R, refer to https://github.com/ahoffrichter/Jabali_et_al_2021_scrRNAseq_analysis. Software and algorithms used for analysis can be seen in Table 6.

PCR analysis

Genomic DNA (for patient mutations and *EML1*-heKO validation) was isolated using the Extractme genomic DNA kit (7Bioscience) according to the manufacturers protocol. Triplicate total mRNA samples were isolated using peqGOLD TriFast (VWR) following the

supplier's instructions. One microgram total mRNA was used for reverse transcription with the iScript cDNA synthesis kit (BioRad) following the manufacturer's protocol. Semi-quantitative PCR reactions were run in at least triplicates using Taq Polymerase (Biozym). PCR conditions and cycle numbers were adjusted to each primer pair for specific DNA amplification on cDNA obtained from commercially available human fetal (single donor, female, 19 weeks of gestation). For quantitative RT-PCR (qRT-PCR), PCR products were assessed by dissociation curve and gel electrophoresis. Data were normalized to 18S rRNA levels. Primers used to validate *EML1*-patient-specific mutations and the *EML1*-heKO as well as *EML1* expression can be seen in Table 7.

Quantitative assessment of 2D and 3D cell cultures

Ectopic neural rosettes were quantified based on NCAD staining and localization in the organoid structure. More precisely, accumulation of NCAD at the basal side of VZ areas was defined as ectopic neural rosettes and quantified per VZ area using the cell counter tool in ImageJ. The percent of VZ areas with ectopic neural rosettes was then calculated for the different conditions. *Organization of neurons* was investigated per cortical area (composed of a VZ and CP area) based on MAPT staining and localization. If the majority of MAPT-positive neurons were found within the CP area, we called them organized. In case MAPT-positive neurons distributed in the CP as well as in the VZ area, we defined that as disorganized. Criteria for heterotopia were met in case clusters or bands of MAPT-positive cells found between the VZ area and the CP region. The percent of heterotopic, disorganized, or organized cortical areas was then calculated for the different conditions. The number and localization of EGFP-positive cells within hybrid organoids were investigated by defining VZ and CP areas and quantifying the EGFP-positive cells in the respective areas using the cell counter tool in ImageJ. *Mitotic planes* were quantified at the VZ surface by analyzing 20- μ m-thick tenner serial sections stained for p-vimentin (to identify dividing cells) and TPX2 (a spindle assembly factor which plays a role in inducing microtubule assembly and growth during M phase used to visualize the plane of dividing

Table 7. Primers used in this study.

Primer	Forward	Reverse	Source
P135 Mut. Exon 5 (T _A 45°C)	GACGTTCTATGTATATATT	TGTTTGATTAGTCCTATAAA	IDT
P135 Mut. Exon 8 (T _A 60°C)	CTGCATGCCTTTGGGG	TGACCGTGTCTGCTAATGC	IDT
3489 Mut. (T _A 60°C)	GCTGGGCACTGAGGTATCTT	ACCACAGCTATTTTCGTCAGGA	IDT
Validation of <i>EML1</i>-heKO:	T _A 60°C for all primer combinations:		
Before Cas. gRNA 1	AGGGAAGAATGATGACAATGAGA		IDT
In Cas. gRNA 1		AAAAGGCGGAGCCAGTACA	IDT
Before Cas. gRNA 2/3	CCTGTTAGCATTGTCCACG		IDT
In Cas. gRNA 2/3		GGAGCGATCGCAGATCCTTG	IDT
<i>EML1</i> WT behind Cas. gRNA 1		TCACTCAAACGCCACCTTT	IDT
<i>EML1</i> WT behind Cas. gRNA 2/3		TTCTTTTCCACTGGAAGAGC	IDT
<i>EML1</i> expression:	T _A 60°C for both pairs:		
<i>EML1</i> -qPCR	GGGTCTATGGGTACAGGGGT	ACTGCTAGGCACTTCACGTC	IDT
18s-qPCR	TTCTTGGACCGCGCAAG	GCCGCATCGCCGGTCGG	IDT

cells). The angle of the spindle of apical radial glia cells in relation to the prospective ventricular surface was investigated using the ImageJ angle tool. *Cell proliferation* at the VZ surface or basal to the VZ areas was quantified based on the distribution of p-Vim-positive cells in the respective localization using the cell counter tool in ImageJ. *BrdU⁺ KI67⁺ cells* at the basal side of the VZ areas were quantified using ImageJ plugin Cell Counter. *PAX6-positive cells displaying nuclear YAP1* were quantified per VZ area following immunohistochemistry. More specifically, the total amount of PAX6-positive cells within a VZ area was determined and divided by the amount of PAX6-positive cells displaying a nuclear YAP1 signal within this area. All quantitative assessments were performed on at least three different organoids derived from at least three independent batches. The *length of the primary cilia* was investigated in cortical progenitors following ARL13B immunostaining using the length measurement tool in ImageJ on three biological replicates. Images for all quantitative assessments were acquired using the confocal microscope Leica TCS SP5II or the fluorescence microscope Leica DM6 B microscope. In order to make the different batches analyzed distinguishable from one another, different shapes and color codes were utilized in the graphs displayed in this study. VZ areas or organoids analyzed from one batch for example are represented by black dots, grey dots, white dots with black border, or grey dots with black border.

Statistical analysis

All quantitative data were generated based on biological triplicates and tested for normal distribution using the D'Agostino & Pearson omnibus normality test. If criteria for normal distribution were met, statistical significance was tested using parametric testing in the form of one-way ANOVA or two-way ANOVA tests followed by *post hoc* testing (Sidak's multiple-comparison test or Tukey's multiple-comparison test) based on the experimental design ($*P < 0.05$, $**P < 0.01$, and $***P < 0.001$). If criteria for normal distribution were not met, non-parametric testing in the form of a two-tailed Mann–Whitney- or Kruskal–Wallis test followed by *post hoc* testing (Dunn's multiple-comparison test) was conducted. All deviations from means are depicted as mean with SD or SEM. All analyses were performed with the help of R statistical software package, IBM SPSS statistics 25, and GraphPad Prism 6. Gene expression was compared between control and *EML1*-heKO cells within cell type using the Wilcoxon rank sum test. Values show Bonferroni-corrected *P*-values ($*P < 0.05$, $**P < 0.01$, and $***P < 0.001$). Comparison of proportion of GO feature sets was performed using the Wilcoxon rank sum test ($*P < 0.05$, $**P < 0.01$, and $***P < 0.001$). Software and algorithms used for analysis can be seen in Table 6.

Generation of schemes

Synopsis image as well as schemes in Figs 2C and EV3A were created using biorender.com.

Data availability

The sc-RNA-seq data will be deposited in NCBI's Gene Expression Omnibus and will be accessible through a GEO Series accession number. For detailed information about the data analysis pipeline in

R and the scRNAseq datasets generated and / or analyzed during the current study, refer to the GitHub repository https://github.com/ahoffrichter/Jabali_et_al_2021_scRNAseq_analysis. Any additional information required to reanalyze the data reported in this study is available from the lead contact upon request.

Expanded View for this article is available online.

Acknowledgements

We thank Nadia Bahi-Buisson, Grazia Mancini, and Anne-Gaëlle Le Moing for their contributions of patient samples, and Carmen Cifuentes-Diaz for her contribution to EM studies. The work was supported by the ERA-NET NEURON, JTC 2015 Neurodevelopmental Disorders, STEM-MCD (to JL), the German research foundation (DFG), Project LA 2933/2-1 (to JL), the French ANR, under the frame of E-Rare-3, the ERA-Net for Research on Rare Diseases (E-RARE18-049, to FF), the French Foundation for Medical Research for a team FRM grant (Equipe FRM to FF), and the generous financial support by the Hector Stiftung II (to PK and JL). Open Access funding enabled and organized by Projekt DEAL.

Author contributions

Ammar Jabali: Data curation; Validation; Investigation; Visualization; Methodology; Writing – original draft; Writing—review & editing. **Anne Hoffrichter:** Data curation; Software; Formal analysis; Investigation; Visualization. **Ana Uzquiano:** Investigation; Methodology. **Fabio Marsoner:** Investigation. **Ruven Wilkens:** Investigation; Visualization; Methodology. **Marco Siekmann:** Validation; Methodology. **Bettina Bohl:** Investigation; Visualization; Methodology. **Andrea, Carlo Rossetti:** Validation. **Sandra Horschitz:** Methodology. **Philipp Koch:** Resources; Funding acquisition; Validation; Writing—original draft; Writing—review & editing. **Fiona Francis:** Resources; Writing—original draft; Writing—review & editing. **Julia Ladewig:** Conceptualization; Resources; Supervision; Funding acquisition; Validation; Investigation; Visualization; Writing—original draft; Writing – review & editing.

In addition to the CRediT author contributions listed above, the contributions in detail are:

JL conceived and designed the research project; AJ, AU, PK, FF, and JL designed experiments; AJ, AU, FM RW, and MS performed experiments and collected data; AJ, AH, AU, BB, ACR, FF, PK, and JL analyzed data; and AJ and SH reprogrammed *EML1* patient samples. FF communicated with clinicians for patient sample collection. FF and PK were involved in ongoing critical discussion. JL and AJ wrote the manuscript with critical help from FF, AU, and PK. All authors provided ongoing critical review of experiments, results, and commented on the manuscript.

Disclosure and competing interest statement

The authors declare that they have no conflict of interest.

References

- Andrews S (2015) FastQC: A Quality Control Tool for High Throughput Sequence Data [Online]. "FastQC," <http://www.bioinformatics.babraham.ac.uk/projects/fastqc/> <https://qubeshub.org/resources/fastqc>
- Ban H, Nishishita N, Fusaki N, Tabata T, Saeki K, Shikamura M, Takada N, Inoue M, Hasegawa M, Kawamata S et al (2011) Efficient generation of transgene-free human induced pluripotent stem cells (iPSCs) by temperature-sensitive Sendai virus vectors. *Proc Natl Acad Sci U S A* 108 (34): 14234–14239

- Bizzotto S, Uzquiano A, Dingli F, Ershov D, Houllier A, Arras G, Richards M, Loew D, Minc N, Croquelois A *et al* (2017) Eml1 loss impairs apical progenitor spindle length and soma shape in the developing cerebral cortex. *Sci Rep* 7(1): 17308
- Camargo FD, Gokhale S, Johnnidis JB, Fu D, Bell GW, Jaenisch R, Brummelkamp TR (2007) YAP1 increases organ size and expands undifferentiated progenitor cells. *Curr Biol* 17(23): 2054–2060
- Cappello S, Gray MJ, Badouel C, Lange S, Einsiedler M, Srour M, Chitayat D, Hamdan FF, Jenkins ZA, Morgan T *et al* (2013) Mutations in genes encoding the cadherin receptor-ligand pair DCHS1 and FAT4 disrupt cerebral cortical development. *Nat Genet* 45(11): 1300–1308
- Collins SC, Uzquiano A, Selloum M, Wendling O, Gaborit M, Osipenko M, Birling MC, Yalcin B, Francis F (2019) The neuroanatomy of Eml1 knockout mice, a model of subcortical heterotopia. *J Anat* 235(3): 637–650
- Eze UC, Bhaduri A, Haeussler M, Nowakowski TJ, Kriegstein AR (2021) Single-cell atlas of early human brain development highlights heterogeneity of human neuroepithelial cells and early radial glia. *Nat Neurosci* 24(4): 584–594
- Fan X, Fu Y, Zhou X, Sun L, Yang M, Wang M, Chen R, Wu Q, Yong J, Dong J *et al* (2020) Single-cell transcriptome analysis reveals cell lineage specification in temporal-spatial patterns in human cortical development. *Sci Adv* 6(34): eaaz2978
- Fietz SA, Lachmann R, Brandl H, Kircher M, Samusik N, Schroder R, Lakshmanaperumal N, Henry I, Vogt J, Riehn A *et al* (2012) Transcriptomes of germinal zones of human and mouse fetal neocortex suggest a role of extracellular matrix in progenitor self-renewal. *Proc Natl Acad Sci U S A* 109(29): 11836–11841
- Hadley W (2016) *Ggplot2*, New York, NY: Springer Science+Business Media LLC
- Iefremova V, Manikakis G, Krefft O, Jabali A, Weynans K, Wilkens R, Marsoner F, Brändl B, Müller F-J, Koch P *et al* (2017) An organoid-based model of cortical development identifies non-cell-autonomous defects in Wnt signaling contributing to Miller-Dieker Syndrome. *Cell Rep* 19(1): 50–59
- Karzbrun E, Kshirsagar A, Cohen SR, Hanna JH, Reiner O (2018) Human brain organoids on a chip reveal the physics of folding. *Nat Phys* 14(5): 515–522
- Kielar M, Tuy FPD, Bizzotto S, Lebrand C, de Juan Romero C, Poirier K, Oegema R, Mancini GM, Bahi-Buisson N, Olaso R *et al* (2014) Mutations in Eml1 lead to ectopic progenitors and neuronal heterotopia in mouse and human. *Nat Neurosci* 17(7): 923–933
- Klinger E, Francis F, Jabaudon D, Cappello S (2021) Mapping the molecular and cellular complexity of cortical malformations. *Science* 371(6527): eaba4517
- Koch P, Siemen H, Biegler A, Itskovitz-Eldor J, Brüstle O (2006) Transduction of human embryonic stem cells by ecotropic retroviral vectors. *Nucleic Acids Res* 34(18): e120
- Kostic M, Paridaen JTML, Long KR, Kalebic N, Langen B, Grübling N, Wimberger P, Kawasaki H, Namba T, Huttner WB (2019) YAP activity is necessary and sufficient for basal progenitor abundance and proliferation in the developing neocortex. *Cell Rep* 27(4): 1103–1118.e6
- Krefft O, Jabali A, Iefremova V, Koch P, Ladewig J (2018) Generation of standardized and reproducible forebrain-type cerebral organoids from human induced pluripotent stem cells. *J Vis Exp* (131): 56768
- LaMonica BE, Lui JH, Hansen DV, Kriegstein AR (2013) Mitotic spindle orientation predicts outer radial glial cell generation in human neocortex. *Nat Commun* 4: 1665
- Liu J, Liu W, Yang LU, Wu Q, Zhang H, Fang AI, Li L, Xu X, Sun LE, Zhang J *et al* (2017) The primate-specific gene TMEM14B marks outer radial glia cells and promotes cortical expansion and folding. *Cell Stem Cell* 21(5): 635–649.e8
- Liu WA, Chen S, Li Z, Lee CH, Mirzaa G, Dobyns WB, Ross ME, Zhang J, Shi SH (2018) PARD3 dysfunction in conjunction with dynamic HIPPO signaling drives cortical enlargement with massive heterotopia. *Genes Dev* 32(11–12): 763–780
- Long KR, Newland B, Florio M, Kalebic N, Langen B, Kolterer A, Wimberger P, Huttner WB (2018) Extracellular matrix components HAPLN1, lumican, and collagen i cause hyaluronic acid-dependent folding of the developing human neocortex. *Neuron* 99(4): 702–719.e6
- Loo L, Simon JM, Xing L, McCoy ES, Niehaus JK, Guo J, Anton ES, Zylka MJ (2019) Single-cell transcriptomic analysis of mouse neocortical development. *Nat Commun* 10(1): 134
- Lui JH, Hansen DV, Kriegstein AR (2011) Development and evolution of the human neocortex. *Cell* 146(1): 18–36
- Martínez-Martínez M, De Juan Romero C, Fernández V, Cárdenas A, Götz M, Borrell V (2016) A restricted period for formation of outer subventricular zone defined by Cdh1 and Trnp1 levels. *Nat Commun* 7: 11812
- Mora-Bermúdez F, Matsuzaki F, Huttner WB (2014) Specific polar subpopulations of astral microtubules control spindle orientation and symmetric neural stem cell division. *eLife* 3: e02875
- Mukhtar T, Breda J, Grison A, Karimaddini Z, Grobecker P, Iber D, Beisel C, van Nimwegen E, Taylor V (2020) Tead transcription factors differentially regulate cortical development. *Sci Rep* 10(1): 4625
- Najas S, Pijuan I, Esteve-Codina A, Usieto S, Martínez JD, Zwijsen A, Arbonés ML, Martí E, Le Dréau G (2020) A SMAD1/5-YAP signalling module drives radial glia self-amplification and growth of the developing cerebral cortex. *Development* 147(13): dev187005
- Nowakowski TJ, Bhaduri A, Pollen AA, Alvarado B, Mostajo-Radji MA, Di Lullo E, Haeussler M, Sandoval-Espinosa C, Liu SJ, Velmeshev D *et al* (2017) Spatiotemporal gene expression trajectories reveal developmental hierarchies of the human cortex. *Science* 358(6368): 1318–1323
- Oegema R, McGillivray G, Leventer R, Le Moing AG, Bahi-Buisson N, Barnicoat A, Mandelstam S, Francis D, Francis F, Mancini GMS *et al* (2019) EML1-associated brain overgrowth syndrome with ribbon-like heterotopia. *Am J Med Genet C Semin Med Genet* 181(4): 627–637
- Oku Y, Nishiya N, Shito T, Yamamoto R, Yamamoto Y, Oyama C, Uehara Y (2015) Small molecules inhibiting the nuclear localization of YAP/TAZ for chemotherapeutics and chemosensitizers against breast cancers. *FEBS Open Bio* 5: 542–549
- O'Neill AC, Kyrousi C, Einsiedler M, Burtscher I, Drukker M, Markie DM, Kirk EP, Götz M, Robertson SP, Cappello S (2018) Mob2 insufficiency disrupts neuronal migration in the developing cortex. *Front Cell Neurosci* 12: 57
- Pollen A, Nowakowski T, Chen J, Retallack H, Sandoval-Espinosa C, Nicholas C, Shuga J, Liu S, Oldham M, Diaz A *et al* (2015) Molecular identity of human outer radial glia during cortical development. *Cell* 163(1): 55–67
- Richards MW, Law EW, Rennalls LP, Busacca S, O'Regan L, Fry AM, Fennell DA, Bayliss R (2014) Crystal structure of EML1 reveals the basis for Hsp90 dependence of oncogenic EML4-ALK by disruption of an atypical β -propeller domain. *Proc Natl Acad Sci U S A* 111(14): 5195–5200
- Richards MW, O'Regan L, Roth D, Montgomery JM, Straube A, Fry AM, Bayliss R (2015) Microtubule association of EML proteins and the EML4-ALK variant 3 oncoprotein require an N-terminal trimerization domain. *Biochem J* 467(3): 529–536
- Sahu MR, Mondal AC (2021) Neuronal Hippo signaling: from development to diseases. *Dev Neurobiol* 81(2): 92–109

- Saito K, Kawasoe R, Sasaki H, Kawaguchi A, Miyata T (2018) Neural progenitor cells undergoing Yap/Tead-mediated enhanced self-renewal form heterotopias more easily in the diencephalon than in the telencephalon. *Neurochem Res* 43(1): 180–189
- Shaheen R, Sebai MA, Patel N, Ewida N, Kurdi W, Altweijri I, Sogaty S, Almadawi E, Seidahmed MZ, Alnemri A et al (2017) The genetic landscape of familial congenital hydrocephalus. *Ann Neurol* 81(6): 890–897
- Shi Y, Kirwan P, Smith J, Robinson HP, Livesey FJ (2012) Human cerebral cortex development from pluripotent stem cells to functional excitatory synapses. *Nat Neurosci* 15(3): pp. 477–86, S1
- Stuart T, Butler A, Hoffman P, Hafemeister C, Papalexi E, Mauck WM, Hao Y, Stoerckius M, Smibert P, Satija R (2019) Comprehensive integration of single-cell data. *Cell* 177(7): 1888–1902.e21
- Uzquiano A, Cifuentes-Diaz C, Jabali A, Romero DM, Houllier A, Dingli F, Maillard C, Boland A, Deleuze JF, Loew D et al (2019) Mutations in the heterotopia gene *Eml1/EML1* severely disrupt the formation of primary cilia. *Cell Rep* 28(6): 1596–1611.e10
- Velasco S, Kedaigle AJ, Simmons SK, Nash A, Rocha M, Quadrato G, Paulsen B, Nguyen L, Adiconis X, Regev A et al (2019) Individual brain organoids reproducibly form cell diversity of the human cerebral cortex. *Nature* 570(7762): 523–527
- Zhang B, Carroll J, Trojanowski JQ, Yao Y, Iba M, Potuzak JS, Hogan A-M L, Xie SX, Ballatore C, Smith AB et al (2012) The microtubule-stabilizing agent, epothilone D, reduces axonal dysfunction, neurotoxicity, cognitive deficits, and Alzheimer-like pathology in an interventional study with aged tau transgenic mice. *J Neurosci* 32(11): 3601–3611
- Zhao B, Tumaneng K, Guan KL (2011) The Hippo pathway in organ size control, tissue regeneration and stem cell self-renewal. *Nat Cell Biol* 13(8): 877–883



License: This is an open access article under the terms of the Creative Commons Attribution-NonCommercial-NoDerivs 4.0 License, which permits use and distribution in any medium, provided the original work is properly cited, the use is non-commercial and no modifications or adaptations are made.